NANO LETTERS

pubs.acs.org/NanoLett

Letter

Continuous Fly-Through High-Temperature Synthesis of Nanocatalysts

Yun Qiao,[‖] Chaoji Chen,[‖] Yang Liu,[‖] Yifan Liu, Qi Dong, Yonggang Yao, Xizheng Wang, Yuyan Shao, Chao Wang, and Liangbing Hu*

Cite This: *Nano Lett.* 2021, 21, 4517−4523

Read Online

ACCESS | Metrics & More | Article Recommendations | Supporting Information

ABSTRACT: The conventional thermal treatment systems typically feature low ramping/cooling rates, which lead to steep thermal gradients that generate inefficient, nonuniform reaction conditions and result in nanoparticle aggregation. Herein, we demonstrate a continuous fly-through material synthesis approach using a novel high-temperature reactor design based on the emerging thermal-shock technology. By facing two sheets of carbon paper with a small distance apart (1−3 mm), uniform and ultrahigh temperatures can be reached up to 3200 K within 50 ms by simply applying a voltage of 15 V. The raw materials can be continuously fed through the device, allowing the final products to be rapidly collected. As a proof-of-concept demonstration, we synthesized Pt nanocatalysts (∼4 nm) anchored on carbon black via this reactor at ∼1400 K. Furthermore, we find it features excellent electrocatalytic activities toward methanol oxidation reaction. This work offers a highly efficient platform for nanomaterials synthesis at high temperatures.

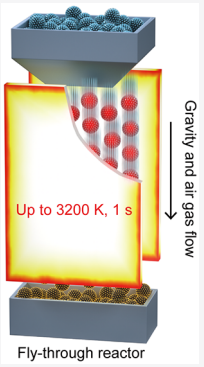

KEYWORDS: *high-temperature synthesis, nanocatalysts, methanol oxidation reaction, energy storage*

INTRODUCTION

Nanomaterials, such as alloys,[1] metallic oxides,[2] and inorganic compounds[3] with narrow particle size distribution and unique physiochemical properties have attracted significant research interest for catalysis,[4] energy storage,[5] and optoelectronic devices.[6] For example, the development of metal nanocatalysts with high activity and durability is mandatory in the field of fuel cells. In order to meet the requirement, numerous synthetic strategies have been developed in recent decades,[7−9] such as electrochemical deposition,[10] solvothermal/hydrothermal method,[11,12] solution combustion,[13] and solid thermolysis.[14,15] However, these conventional synthetic routes generally suffer from long sintering time, high energy consumption, complex procedures, or critical reaction conditions.[16−19]

Meanwhile, thermal treatment is an important approach to achieve metal nanocatalysts from the salt precursors, while the particles are prone to aggregate during the long heating process.[20−23] As we know, traditional muffle and tube furnaces with convective heating can transfer heat from the heated mantle to the reactant precursors.[24−27] However, the low ramping and cooling rates (generally <100 K min^{-1}) tend to result in large thermal gradients through the bulk reactant and therefore uneven reaction conditions.[28−31] This is a commonly encountered problem during nanomaterials synthesis, particularly when scaled-up, as nanoparticles tend to aggregate with a broad size distribution due to their large surface energies at high temperatures and long reaction time.[32−34] Recently, thermal-shock technology was proposed to overcome the limitation of low ramping/cooling rates of traditional methods.[35−37] The ultrahigh ramping/cooling rates (up to 10^5 K s^{-1}) enable the rapid synthesis of well-dispersed ultrafine nanoparticles. Despite these advantages, it remains challenging to achieve continuous, scale-up synthesis of nanoparticles using this thermal-shock technology, as generally this method is not continuous in synthesis and relies on the materials being conductive films.

Herein, we demonstrate a continuous fly-through high-temperature reactor (up to ∼3200 K) for the synthesis of supported nanoparticles. This method can not only apply to the high-temperature synthesis of materials being powders but also accomplish the continuous synthesis of nanoparticles. The reactor features a simple design of two face-to-face carbon paper films separated by a small distance (1−3 mm), which can generate ultrahigh temperatures via Joule-heating. By flowing metal salt precursors on carbon between these heating sheets under gravity and the carrier gas, the high temperature rapidly decomposes these raw materials into metal nanoparticles anchored on the carbon substrate (e.g., porous carbon black particles). In this way, we are able to continuously produce homogeneous nanocatalysts at a large scale, as shown schemati-

Received: September 7, 2020
Revised: April 13, 2021
Published: May 21, 2021

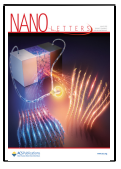

https://doi.org/10.1021/acs.nanolett.0c03620
Nano Lett. 2021, 21, 4517−4523

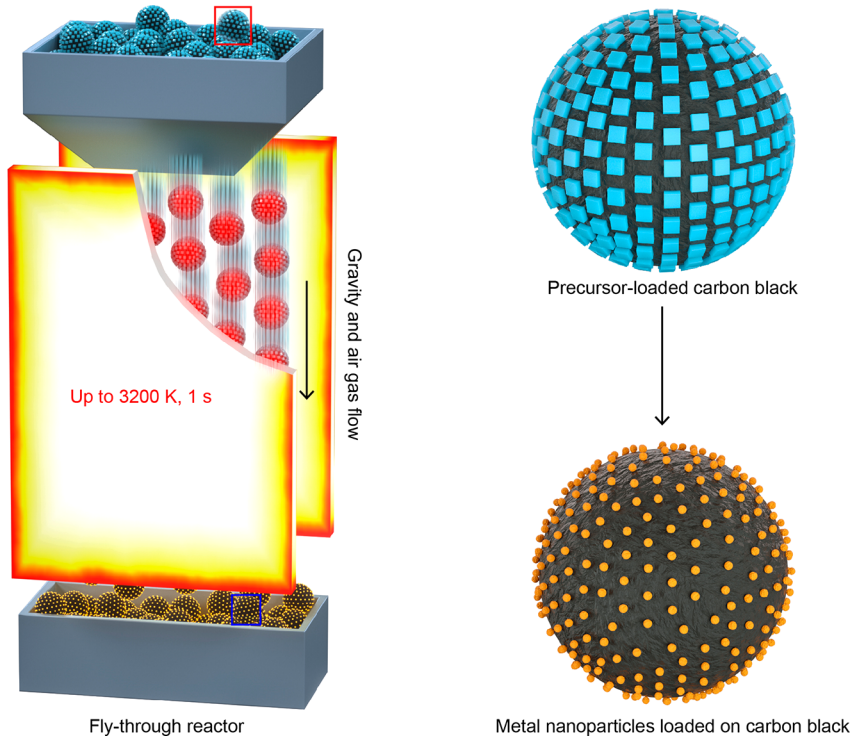

Figure 1. Schematic illustration of the fly-through high-temperature reactor, in which raw materials (precursor loaded carbon black (CB) powder) rapidly flow down between two joule-heated carbon sheets under the force of gravity and the carrier air gas. The precursor salts are *in situ* thermally decomposed to metallic nanoparticles uniformly anchored on carbon black.

cally in Figure 1. This reactor features a large reaction space, a uniform, controlled temperature distribution, and continuous heating, enabling ultrafast decomposition of diverse precursors for a universal process. As a proof-of-concept demonstration, we synthesized Pt nanoparticles anchored on carbon black via this continuous fly-through high-temperature reactor at a temperature of 1400 K. We can use methanol oxidation to evaluate the resulting Pt nanoparticles (~4 nm in size) as an anodic catalyst, in which we observed excellent electrocatalytic activity and stability. This work sheds light on the rapid yet versatile strategy for the fabrication of monodispersed and size-controlled nanocatalysts for direct methanol fuel cell and other renewable energy storage technologies.

The reaction setup (90 mm × 60 mm × 3.6 mm) was assembled using glass slides, copper foil, and carbon paper, as shown in Figure S1a. The glass slides serve to constitute the framework of the reactor, in which we adhere to a layer of copper foil to rapidly dissipate heat and protect the reactor structure. We then attached two layers of carbon paper (0.19 mm thick) to the two sides of the reactor framework with silver paste, used the glass slides to fix the top and down sides, and then covered a layer of copper foil to be the conductive poles. The schematic diagram of the fly-through high-temperature reactor is pictured in Figure S1b. The carbon paper, as an effective blackbody, is a principal component of the reactor and can serve as a radiative heating source.

Figure 2a displays an optical photograph of the working reactor under high temperature. An electrical input power source was adopted to control the temperature and heating time of the reactor. We measured the spatial temperature distribution of the reactor by a high-speed camera recorded at 4000 frames per second, which allowed us to estimate the temperature to be ~2300 K according to the color ratio pyrometry technique (see Methods for details, Supporting Information).[38] By changing the voltage applied to the two carbon sheets, we demonstrated the reactor could achieve temperatures ranging from 1100−3200 K during the joule heating process (Figure 2b), as indicated by the increasing light emission with the higher input current. Figure S2a further shows the reactor's temperature over time, in which it rapidly increased to 2000 K within 50 ms and remained at 2300 K for about 200 ms. When we shut the power supply off, the reaction temperature decreased to 1500 K within 25 ms. Accordingly, we calculated the heating and cooling rates to be as high as 10^4 K s^{-1}. Figure 2c displays the recorded temperature vs time curve for the reactor at 3200 K.

We used an optical fiber at the side of the reactor to capture the thermal radiation spectra so as to further detect the temperature and cycling performance of the reactor, as shown in Figure 2d−f and Figure S2. Figure 2d illustrates a typical time-controlled trajectory of the reactor for about 1 s, where the working procedure of the reactor can be clearly divided into three stages: a rapid temperature ramping step, a short and stable temperature holding process, and an instantaneous cooling process. In addition, the thermal radiation source of carbon paper can work continuously for 60 min without any degradation, indicating its excellent thermal stability under the high temperature (Figure 2e). The cycling performance of the reactor is shown in Figure 2f in which the light emission curves maintain the same shape, suggesting the excellent stability of the reactor even after 600 cycles.

We further characterized the carbon paper with dimensions of 67 mm × 7 mm × 0.17 mm in the fly-through high-temperature reactor. We monitored the temperature distribution for the carbon paper under a current pulse (a low temperature) in the air by an infrared radiation (IR) camera (Figure 3a). The temperature obtained from the carbon paper increased from

https://doi.org/10.1021/acs.nanolett.0c03620
Nano Lett. 2021, 21, 4517−4523

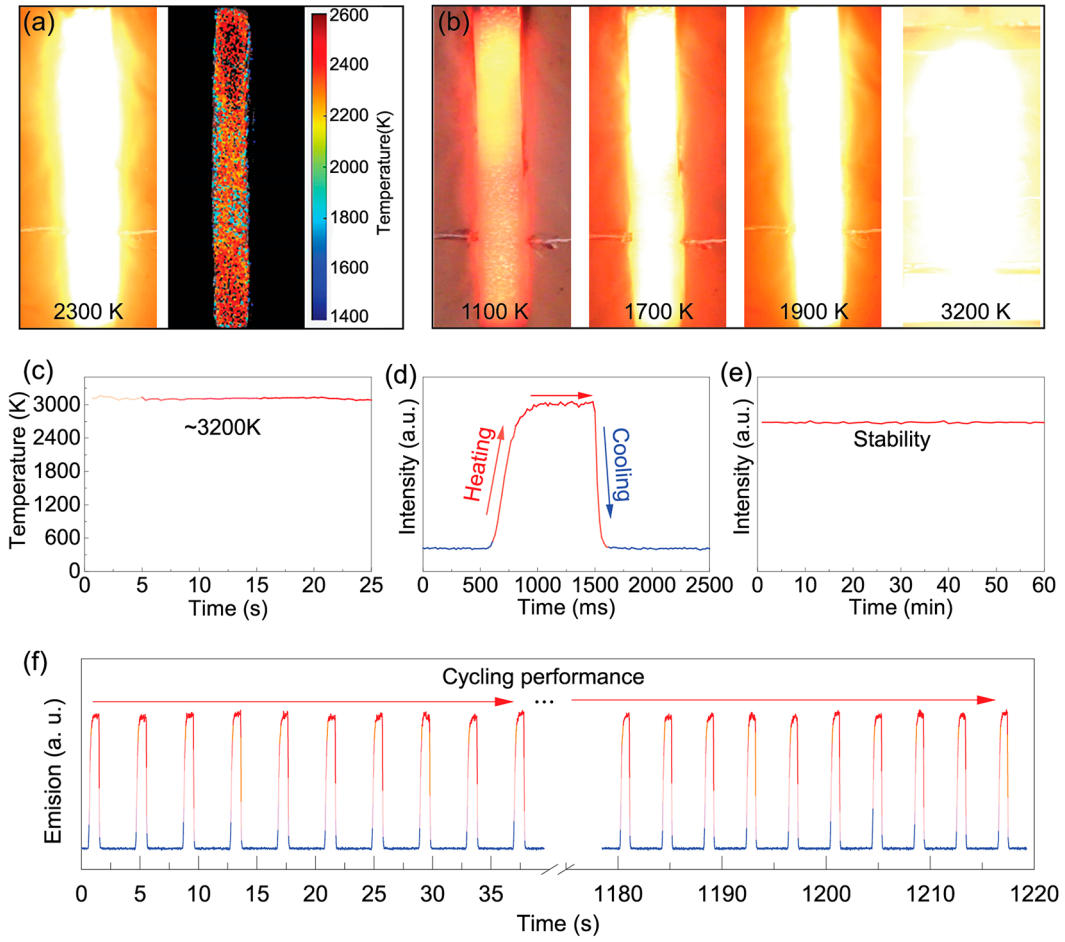

Figure 2. High-temperature properties of the fly-through reactor. (a) Optical photograph and corresponding spatial temperature distribution image of the reactor at 2300 K. (b) Photographs of a typical reactor under various temperatures. (c) The temperature versus time curve of a typical reactor heating at 3200 K. (d) The temporal evolution of light intensity for the 1 s joule heating process. (e) The stability and (f) the cycling performance of the reactor.

room temperature to ~570 K. Notably, the heat distributed effectively throughout the entire carbon paper. These results indicate that carbon paper as the reactor's principal component serves as a highly effective thermal radiation source, which could help promote chemical reaction for material synthesis. We also measured the mechanical properties of the carbon paper via tensile testing to evaluate its reliability (Figure 3b). The stress−strain curve of the carbon paper displays linear deformation behavior before tensile failure. Compared with the plastics, the strength of the reactor heating source is high enough for the fly through high-temperature synthesis of nanomaterials (Figure 3c).[39,40]

The optical photographs in Figure 3d,e for the carbon paper before and after heating to over 3000 K for 10 min indicate the shape and bendability of carbon paper can be maintained after the heating to over 3000 K for 10 min. We also investigated the stability of the carbon paper by scanning electron microscopy (SEM). As shown in Figure 3f, the original carbon paper is composed of entangled carbon fibers of 6−9 μm in diameter. The interconnected carbon fibers provide a conductive network, facilitating electron transport and thermal conduction throughout the material, which is critical to achieving rapid heating/cooling rates and uniform temperature distribution with a small temperature gradient. High-magnification SEM imaging reveals these carbon fibers consist of gullies and trenches on the surface. After Joule heating to over 3000 K, we examined the morphology of the carbon paper by SEM again. Compared with the original morphology, there is no obvious structural change (Figure 3g) of the carbon fiber, indicating the good stability of the carbon fibers and the carbon paper overall as a high-temperature heating source.

To understand the practicality of this continuous fly-through high-temperature reactor, we demonstrated the preparation of Pt nanoparticles anchored on carbon black under high-temperature conditions (Figure S3). Figure 4a shows the commercial carbon black, which consists of a large number of spherical-like particles (Figure 4b). After mixing with Pt salt solution and subsequent freeze-drying, the morphology of Pt salt-carbon black precursor maintained the original morphology of carbon black without observable changes (Figure 4c). We set the working temperature of the reactor to be 1400 K by adjusting the input current (Figure 4d). The temperature over time of the reactor is shown in Figure S4. The reactants then flew down through the high-temperature reactor under the force of gravity and carrier air gas (Figure 4d), allowing the reacted products to be easily collected from the outlet (Figure 4e).

We investigated the morphology of the as-resulted Pt nanoparticles anchored on the carbon black (Pt NP/C) using SEM (Figure 4f) in which the product is composed of a large number of spherical-like particles approximately 40 nm in size,

https://doi.org/10.1021/acs.nanolett.0c03620
Nano Lett. 2021, 21, 4517−4523

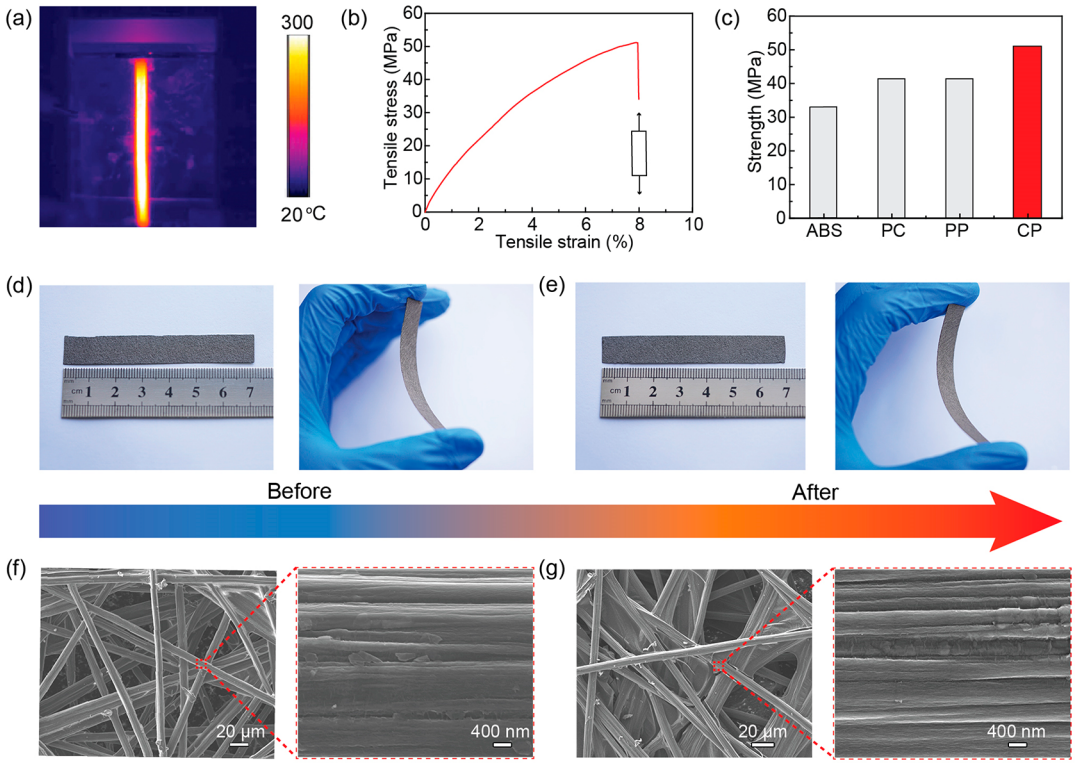

Figure 3. Stability and structural properties of the carbon paper as the principle thermal radiation component of the reactor. (a) IR temperature distribution mapping image of the reactor under a low current pulse. (b) The stress−strain curve of the carbon paper. (c) Comparison of the tensile strength of the carbon paper with other materials, such as acrylonitrile−butadiene−styrene copolymer (ABS), polycarbonate (PC), and polypropylene (PP). Optical photographs and SEM images of the carbon paper (d,f) before heating and (e,g) after heating to over 3000 K for 10 min.

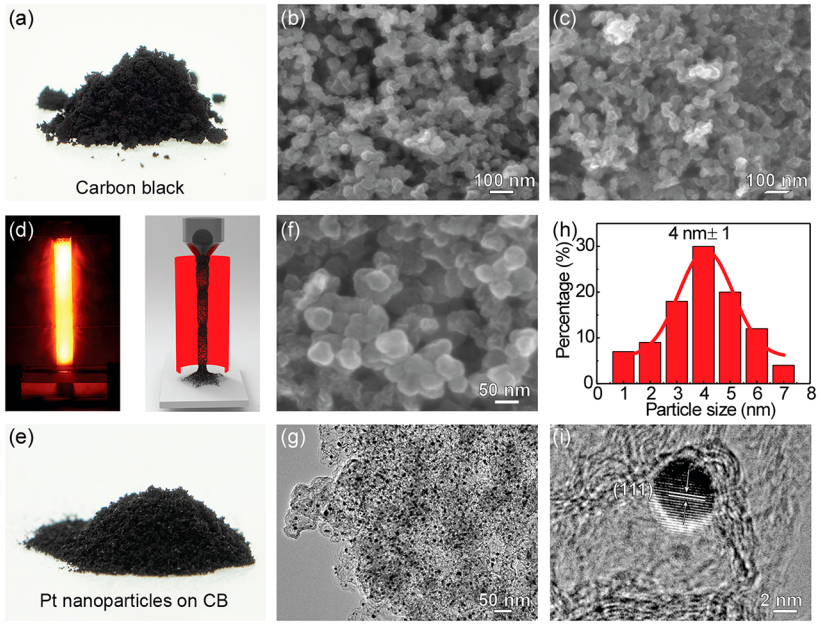

Figure 4. Continuous fly-through synthesis of Pt nanoparticles anchored on carbon black using the home-built high-temperature reactor. (a) Digital photograph of carbon black. SEM images of (b) carbon black, and (c) carbon black coated with Pt salts. (d) Photograph image and schematic illustration of the synthesis of Pt nanoparticles anchored on carbon black at ~1400 K using the high-temperature reactor. (e) Digital photograph, (f) SEM image, and (g) TEM image of the Pt NP/C synthesized using the fly-through high-temperature reactor. (h) Histogram of the Pt nanoparticle size distribution. (i) High-resolution TEM of Pt NP/C.

which mainly correspond to carbon black, while the Pt nanoparticles could not be observed. However, transmission electron microscopy (TEM) images show the uniformly dispersed Pt nanoparticles on the carbon black substrate (Figure 4g), which were an average of ~4 nm in size (Figure 4h). The high-resolution TEM image in Figure 4i reveals a lattice fringe spacing of ~0.23 nm, corresponding to the (111) plane of cubic Pt (JCPDS No. 87-0646). Moreover, inductively coupled

https://doi.org/10.1021/acs.nanolett.0c03620
Nano Lett. 2021, 21, 4517−4523

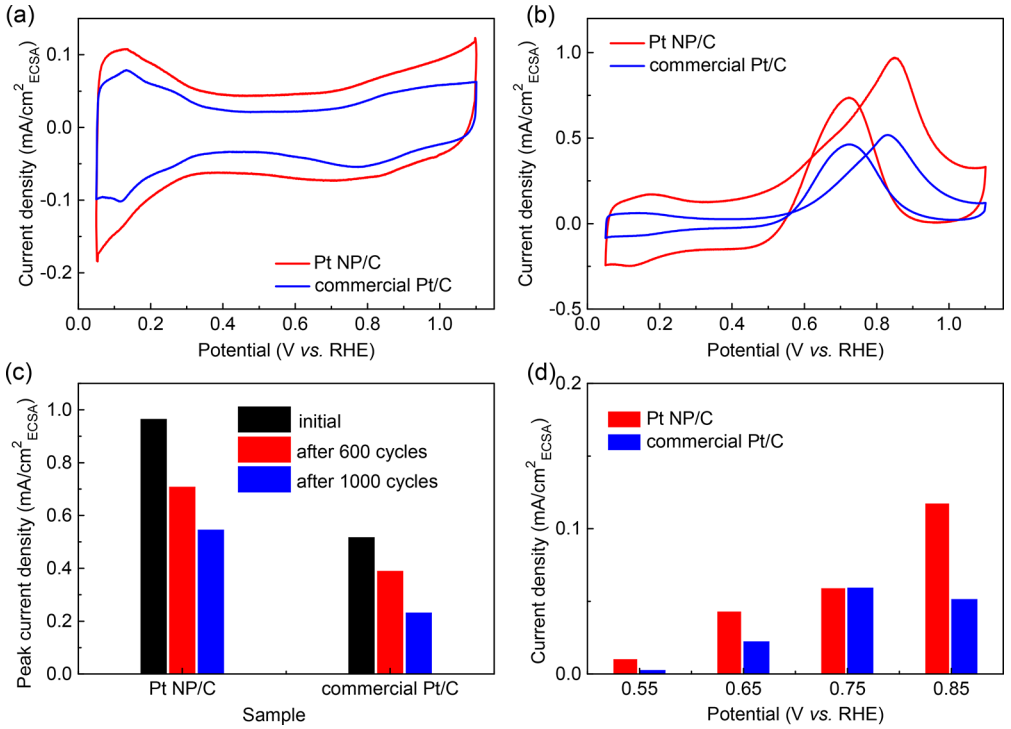

Figure 5. (a) CV curves of the Pt NP/C sample synthesized by the fly-through high-temperature reactor compared to that of commercial Pt/C in 0.1 M $HClO_4$. (b) The CV and (c) peak current density after certain cycles and the (d) average chronoamperometry current density of both samples in 0.1 M $HClO_4$ + 0.1 M methanol electrolyte.

plasma (ICP) analysis was utilized and the Pt loading in Pt NP/C is calculated to be 13.0 wt %, which is consistent with the energy-dispersive X-ray (EDX) result (14.0 wt %). In addition, Pt NP/C-HT was synthesized at a relatively high temperature (~1700 K), and the Pt particle size is ~7 nm (Figure S5). From the results, we can conclude that the fly-through high-temperature reactor is able to synthesize ultrasmall nanomaterials in a highly efficient and continuous manner. We anticipate that more universal metal or alloy nanocatalysts can be synthesized through this continuous fly-through high-temperature treating process via altering the carbon substrate, salt precursors, the reaction temperature, and/or time.

We further tested the electrocatalytic performance of the Pt NP/C synthesized via the fly-through method, as shown in Figure 5. The Pt NP/C possesses typical cyclic voltammogram (CV) curves similar to that of commercial Pt/C (Figure 5a) with a hydrogen underpotential deposition (Hupd) peak in the potential range of 0.05−0.4 V and an OH adsorption peak in the potential region of 0.7−1.1 V. The Pt loading is kept identical (~30 ug/cm$^2_{geo}$) for both the Pt NP/C and commercial Pt/C materials, the electrochemical active surface area (ECSA) values derived from the Hupd region are 1.63 and 1.42 cm^2 (27.7 m^2/g $_{Pt}$ and 24.1 m^2/g $_{Pt}$) for Pt NP/C and commercial Pt/C, respectively. Notably, when tested in the same 0.1 M $HClO_4$ + 0.1 M methanol electrolyte, the Pt NP/C shows significantly enhanced methanol oxidation reaction (MOR) activity and stability compared to those of the commercial Pt/C, as shown in Figure 5b. Pt NP/C possesses an onset potential at 0.35 V, which is ~120 mV lower than that of the commercial Pt/C. Meanwhile, the peak current of Pt NP/C is almost two times higher than that of the commercial Pt/C (1.05 mA/cm$^2_{ECSA}$ versus 0.55 mA/cm$^2_{ECSA}$). The ECSA and peak current for the as-obtained Pt NP/C-HT sample are 1.53 cm^2 and 0.92 mA/cm$^2_{ECSA}$, respectively, the performance is higher than that of commercial Pt/C but lower than that of Pt NP/C (Figure S7).

Moreover, Pt NP/C also exhibits enhanced stability for MOR, in which the corresponding peak current is 0.55 mA/cm$^2_{ECSA}$ after 1000 cycles with a higher current retention of 56.5% in comparison to a retention of 44.8% by the commercial Pt/C under the same testing conditions (Figure 5c). Notably, the CV curves of the Pt NP/C sample tested at different times, also the chronoamperometry current densities of the samples and the corresponding error bars are shown in Figure S6, indicating the measurement results are repeatable. Finally, Figure 5d shows the average current of the samples during chronoamperometry measurements, in which Pt NP/C is significantly superior to commercial Pt/C. For example, Pt NP/C showed 3.7- and 1.9-fold improvement in the current density compared to the commercial Pt/C at 0.55 and 0.65 V, respectively. The above results indicate that the Pt NP/C possesses a better methanol oxidation performance than that of commercial Pt/C, further confirming the effectiveness of our fly-through high-temperature synthesis method for high-performance nanocatalysts production.

CONCLUSION

In this study, we have demonstrated a novel continuous fly through reactor for nanomaterial synthesis at ultrahigh reaction temperatures of up to 3200 K. The reactor allows raw materials to be reacted at high temperature in a continuous manner for the rapid synthesis of nanomaterials at large scale. The reaction temperature can be controlled by simply tuning the input current. As a proof-of-concept demonstration, we successfully synthesized a large amount of Pt nanoparticles anchored on carbon black with an average size of ~4 nm at ~1400 K in a rapid and continuous fashion. The resulting Pt nanoparticles

https://doi.org/10.1021/acs.nanolett.0c03620
Nano Lett. 2021, 21, 4517−4523

anchored on carbon black exhibited enhanced electrocatalytic activity and stability in the methanol oxidation reaction, demonstrating superior capability compared with the commercial Pt/C electrocatalyst. This approach can be extended to the synthesis of other metal nanocatalysts beyond Pt, such Ru, Ir, Ni, Co, and their corresponding metal alloys, providing a feasible and convenient strategy for the continuous high-temperature synthesis of nanomaterials for energy application and beyond.

■ ASSOCIATED CONTENT

Supporting Information

. The Supporting Information is available free of charge at https://pubs.acs.org/doi/10.1021/acs.nanolett.0c03620.

Experimental methods; schematic illustration of the heater; the temperature test of the reactor over time; digital photographs of the reactor; repeatability of the electrochemical performance; characterizations on the Pt NP/C-HT sample synthesized at a relatively high temperature (PDF)

■ AUTHOR INFORMATION

Corresponding Author

Liangbing Hu − *Department of Materials Science and Engineering, University of Maryland, College Park, Maryland 20742, United States;* orcid.org/0000-0002-9456-9315; Email: binghu@umd.edu

Authors

Yun Qiao − *Department of Materials Science and Engineering, University of Maryland, College Park, Maryland 20742, United States*

Chaoji Chen − *Department of Materials Science and Engineering, University of Maryland, College Park, Maryland 20742, United States;* orcid.org/0000-0001-9553-554X

Yang Liu − *Department of Materials Science and Engineering, University of Maryland, College Park, Maryland 20742, United States*

Yifan Liu − *Department of Chemical and Biomolecular Engineering, Johns Hopkins University, Baltimore, Maryland 21218, United States*

Qi Dong − *Department of Materials Science and Engineering, University of Maryland, College Park, Maryland 20742, United States*

Yonggang Yao − *Department of Materials Science and Engineering, University of Maryland, College Park, Maryland 20742, United States*

Xizheng Wang − *Department of Materials Science and Engineering, University of Maryland, College Park, Maryland 20742, United States*

Yuyan Shao − *Pacific Northwest National Laboratory, Richland, Washington 99352, United States;* orcid.org/0000-0001-5735-2670

Chao Wang − *Department of Chemical and Biomolecular Engineering, Johns Hopkins University, Baltimore, Maryland 21218, United States;* orcid.org/0000-0001-7398-2090

Complete contact information is available at: https://pubs.acs.org/10.1021/acs.nanolett.0c03620

Author Contributions

‖Y.Q., C.C., and Yang Liu contributed equally to this work.

Author Contributions

L.H., Y.Q., and Yang Liu conceived the idea and designed the experiments. Y.Q. and Yang Liu contributed to the sample preparation, SEM, and TEM images. Yifan Liu and C.W. conducted the electrochemical performance test. Yang Liu was responsible for the mechanical test. Y.Q., Yang Liu, C.C., Y.S., and L.H. contributed to the analysis and discussion of all data and wrote the manuscript collaboratively. All authors commented on the final manuscript.

Notes

The authors declare no competing financial interest.

■ ACKNOWLEDGMENTS

This work is supported by the NSF Scalable Nanomanufacturing Project (No. 1635221). We acknowledge the support of the Maryland Nanocenter, its Surface Analysis Center, and AIMLab. We would like to express our thanks for funding from the Maryland Innovation Initiative and TEDCO. We appreciate the great help from Yong Pei and Bao Yang for the IR temperature test. We are grateful for Jiaqi Dai's suggestion on the schematic illustration. Y.S. acknowledges the support of Chemical Transformation Initiative at the Pacific Northwest National Laboratory.

■ REFERENCES

(1) Chen, P.-C.; Liu, M.; Du, J. S.; Meckes, B.; Wang, S.; Lin, H.; Dravid, V. P.; Wolverton, C.; Mirkin, C. A. Interface and Heterostructure Design in Polyelemental Nanoparticles. *Science* **2019**, *363* (6430), 959−964.

(2) Zavabeti, A.; Ou, J. Z.; Carey, B. J.; Syed, N.; Orrell-Trigg, R.; Mayes, E. L. H.; Xu, C.; Kavehei, O.; O'Mullane, A. P.; Kaner, R. B.; Kalantar-Zadeh, K.; Daeneke, T. A liquid Metal Reaction Environment for the Room-Temperature Synthesis of Atomically Thin Metal Oxides. *Science* **2017**, *358* (6361), 332−335.

(3) Sun, W.; Dacek, S. T.; Ong, S. P.; Hautier, G.; Jain, A.; Richards, W. D.; Gamst, A. C.; Persson, K. A.; Ceder, G. The Thermodynamic Scale of Inorganic Crystalline Metastability. *Sci. Adv.* **2016**, *2* (11), e1600225.

(4) Zhang, M.; Dai, Q.; Zheng, H.; Chen, M.; Dai, L. Novel MOF-Derived Co@N-C Bifunctional Catalysts for Highly Efficient Zn-Air Batteries and Water Splitting. *Adv. Mater.* **2018**, *30* (10), 1705431.

(5) Chmiola, J.; Yushin, G.; Gogotsi, Y.; Portet, C.; Simon, P.; Taberna, P. L. Anomalous Increase in Carbon Capacitance at Pore Sizes Less Than 1 Nanometer. *Science* **2006**, *313* (5794), 1760−1763.

(6) Wang, Q. H.; Kalantar-Zadeh, K.; Kis, A.; Coleman, J. N.; Strano, M. S. Electronics and Optoelectronics of Two-Dimensional Transition Metal Dichalcogenides. *Nat. Nanotechnol.* **2012**, *7*, 699.

(7) Xue, S.; Deng, W.; Yang, F.; Yang, J.; Amiinu, I. S.; He, D.; Tang, H.; Mu, S. Hexapod PtRuCu Nanocrystalline Alloy for Highly Efficient and Stable Methanol Oxidation. *ACS Catal.* **2018**, *8* (8), 7578−7584.

(8) Bao, M.; Amiinu, I. S.; Peng, T.; Li, W.; Liu, S.; Wang, Z.; Pu, Z.; He, D.; Xiong, Y.; Mu, S. Surface Evolution of PtCu Alloy Shell over Pd Nanocrystals Leads to Superior Hydrogen Evolution and Oxygen Reduction Reactions. *ACS Energy Lett.* **2018**, *3* (4), 940−945.

(9) Li, M.; Carter, R.; Douglas, A.; Oakes, L.; Pint, C. L. Sulfur Vapor-Infiltrated 3D Carbon Nanotube Foam for Binder-Free High Areal Capacity Lithium-Sulfur Battery Composite Cathodes. *ACS Nano* **2017**, *11* (5), 4877−4884.

(10) Tiwari, J. N.; Sultan, S.; Myung, C. W.; Yoon, T.; Li, N.; Ha, M.; Harzandi, A. M.; Park, H. J.; Kim, D. Y.; Chandrasekaran, S. S.; Lee, W. G.; Vij, V.; Kang, H.; Shin, T. J.; Shin, H. S.; Lee, G.; Lee, Z.; Kim, K. S. Multicomponent Electrocatalyst with Ultralow Pt Loading and High Hydrogen Evolution Activity. *Nat. Energy* **2018**, *3* (9), 773−782.

(11) Ding, J.; Zhang, H.; Zhou, H.; Feng, J.; Zheng, X.; Zhong, C.; Paek, E.; Hu, W.; Mitlin, D. Sulfur-Grafted Hollow Carbon Spheres for Potassium-Ion Battery Anodes. *Adv. Mater.* **2019**, *31* (30), 1900429.

(12) Zhang, J.; Zhao, X.; Du, L.; Li, Y.; Zhang, L.; Liao, S.; Goodenough, J. B.; Cui, Z. Antiperovskite Nitrides $CuNCo_{3-x}V_x$: Highly Efficient and Durable Electrocatalysts for the Oxygen-Evolution Reaction. *Nano Lett.* **2019**, *19* (10), 7457−7463.
(13) Thoda, O.; Xanthopoulou, G.; Vekinis, G.; Chroneos, A. Review of Recent Studies on Solution Combustion Synthesis of Nanostructured Catalysts. *Adv. Eng. Mater.* **2018**, *20* (8), 1800047.
(14) Qin, X.; Zhu, S.; Xiao, F.; Zhang, L.; Shao, M. Active Sites on Heterogeneous Single-Iron-Atom Electrocatalysts in CO_2 Reduction Reaction. *ACS Energy Lett.* **2019**, *4* (7), 1778−1783.
(15) Qiao, Y.; Wu, J.; Zhao, J.; Li, Q.; Zhang, P.; Hao, C.; Liu, X.; Yang, S.; Liu, Y. Synergistic Effect of Bifunctional Catalytic Sites and Defect Engineering for High-Performance Li-CO_2 Batteries. *Energy Storage Mater.* **2020**, *27*, 133−139.
(16) Mullinger, P.; Jenkins, B. *Industrial and Process Furnaces: Principles, Design and Operation*, 2nd ed.; Butterworth-Heinemann: Oxford, 2014.
(17) Pu, Z.; Zhao, J.; Amiinu, I. S.; Li, W.; Wang, M.; He, D.; Mu, S. A Universal Synthesis Strategy for P-Rich Noble Metal Diphosphide-Based Electrocatalysts for the Hydrogen Evolution Reaction. *Energy Environ. Sci.* **2019**, *12* (3), 952−957.
(18) Li, J.-C.; Xiao, F.; Zhong, H.; Li, T.; Xu, M.; Ma, L.; Cheng, M.; Liu, D.; Feng, S.; Shi, Q.; Cheng, H.-M.; Liu, C.; Du, D.; Beckman, S. P.; Pan, X.; Lin, Y.; Shao, M. Secondary-Atom-Assisted Synthesis of Single Iron Atoms Anchored on N-Doped Carbon Nanowires for Oxygen Reduction Reaction. *ACS Catal.* **2019**, *9* (7), 5929−5934.
(19) Lu, X.; Wu, Y.; Yuan, X.; Huang, L.; Wu, Z.; Xuan, J.; Wang, Y.; Wang, H. High-Performance Electrochemical CO_2 Reduction Cells Based on Non-noble Metal Catalysts. *ACS Energy Lett.* **2018**, *3* (10), 2527−2532.
(20) Qin, X.; Zhang, L.; Xu, G.-L.; Zhu, S.; Wang, Q.; Gu, M.; Zhang, X.; Sun, C.-J.; Balbuena, P. B.; Amine, K.; Shao, M. The Role of Ru in Improving the Activity of Pd toward Hydrogen Evolution and Oxidation Reactions in Alkaline Solutions. *ACS Catal.* **2019**, *9* (10), 9614−9621.
(21) Zhong, Y.; Yin, L.; He, P.; Liu, W.; Wu, Z.; Wang, H. Surface Chemistry in Cobalt Phosphide-Stabilized Lithium-Sulfur Batteries. *J. Am. Chem. Soc.* **2018**, *140* (4), 1455−1459.
(22) Wu, Y.; Cao, S.; Hou, J.; Li, Z.; Zhang, B.; Zhai, P.; Zhang, Y.; Sun, L. Rational Design of Nanocatalysts with Nonmetal Species Modification for Electrochemical CO_2 Reduction. *Adv. Energy Mater.* **2020**, *10* (29), 2000588.
(23) Ma, C.; Wei, H.-F.; Wang, M.-X.; Wu, S.; Chang, Y.-C.; Zhang, J.; Jiang, L.-P.; Zhu, W.; Chen, Z.; Lin, Y. Hydrogen Evolution Reaction Monitored by Electrochemiluminescence Blinking at Single-Nanoparticle Level. *Nano Lett.* **2020**, *20* (7), 5008−5016.
(24) Cohn, A. P.; Share, K.; Carter, R.; Oakes, L.; Pint, C. L. Ultrafast Solvent-Assisted Sodium Ion Intercalation into Highly Crystalline Few-Layered Graphene. *Nano Lett.* **2016**, *16* (1), 543−8.
(25) Li, X.; Zhang, K.; Mitlin, D.; Paek, E.; Wang, M.; Jiang, F.; Huang, Y.; Yang, Z.; Gong, Y.; Gu, L.; Zhao, W.; Du, Y.; Zheng, J. Li-Rich $Li[Li_{1/6}Fe_{1/6}Ni_{1/6}Mn_{1/2}]O_2$ (LFNMO) Cathodes: Atomic Scale Insight on the Mechanisms of Cycling Decay and of the Improvement due to Cobalt Phosphate Surface Modification. *Small* **2018**, *14* (40), 1802570.
(26) Share, K.; Cohn, A. P.; Carter, R.; Rogers, B.; Pint, C. L. Role of Nitrogen-Doped Graphene for Improved High-Capacity Potassium Ion Battery Anodes. *ACS Nano* **2016**, *10* (10), 9738−9744.
(27) Wu, Z.; Huang, L.; Liu, H.; Wang, H. Element-Specific Restructuring of Anion- and Cation-Substituted Cobalt Phosphide Nanoparticles under Electrochemical Water-Splitting Conditions. *ACS Catal.* **2019**, *9* (4), 2956−2961.
(28) Chen, C.; Chen, Y.; Zhu, S.; Dai, J.; Pastel, G.; Yao, Y.; Liu, D.; Wang, Y.; Wan, J.; Li, T.; Luo, W.; Hu, L. Catalyst-Free In Situ Carbon Nanotube Growth in Confined Space via High Temperature Gradient. *Research* **2018**, *2018*, 1.
(29) Ding, J.; Zhou, H.; Zhang, H.; Tong, L.; Mitlin, D. Selenium Impregnated Monolithic Carbons as Free-Standing Cathodes for High Volumetric Energy Lithium and Sodium Metal Batteries. *Adv. Energy Mater.* **2018**, *8* (8), 1701918.
(30) Meng, C.; Muralidharan, N.; Teblum, E.; Moyer, K. E.; Nessim, G. D.; Pint, C. L. Multifunctional Structural Ultrabattery Composite. *Nano Lett.* **2018**, *18* (12), 7761−7768.
(31) Qiao, Y.; Xu, S.; Liu, Y.; Dai, J.; Xie, H.; Yao, Y.; Mu, X.; Chen, C.; Kline, D. J.; Hitz, E.; Liu, B.; Song, J.; He, P.; Zachariah, M.; Hu, L. Transient, in situ Synthesis of Ultrafine Ruthenium Nanoparticles for a High-rate Li-CO_2 Battery. *Energy Environ. Sci.* **2019**, *12*, 1100−1107.
(32) Wang, H.; Huang, X.; Li, W.; Gao, J.; Xue, H.; Li, R. K. Y.; Mai, Y.-W. TiO_2 Nanoparticle Decorated Carbon Nanofibers for Removal of Organic Dyes. *Colloids Surf., A* **2018**, *549*, 205−211.
(33) Yeom, S. J.; Lee, C.; Kang, S.; Wi, T.-U.; Lee, C.; Chae, S.; Cho, J.; Shin, D. O.; Ryu, J.; Lee, H.-W. Native Void Space for Maximum Volumetric Capacity in Silicon-Based Anodes. *Nano Lett.* **2019**, *19* (12), 8793−8800.
(34) Fan, F.; Liu, Z.; Sun, M.; Nichols, P. L.; Turkdogan, S.; Ning, C. Z. Mid-Infrared Lasing in Lead Sulfide Subwavelength Wires on Silicon. *Nano Lett.* **2020**, *20* (1), 470−477.
(35) Yao, Y.; Huang, Z.; Xie, P.; Lacey, S. D.; Jacob, R. J.; Xie, H.; Chen, F.; Nie, A.; Pu, T.; Rehwoldt, M.; Yu, D.; Zachariah, M. R.; Wang, C.; Shahbazian-Yassar, R.; Li, J.; Hu, L. Carbothermal Shock Synthesis of High-Entropy-Alloy Nanoparticles. *Science* **2018**, *359* (6383), 1489−1494.
(36) Wu, M.; Cui, M.; Wu, L.; Hwang, S.; Yang, C.; Xia, Q.; Zhong, G.; Qiao, H.; Gan, W.; Wang, X.; Kline, D.; Zachariah, M. R.; Su, D.; Li, T.; Hu, L. Hierarchical Polyelemental Nanoparticles as Bifunctional Catalysts for Oxygen Evolution and Reduction Reactions. *Adv. Energy Mater.* **2020**, *10* (25), 2001119.
(37) Chen, Y.; Egan, G. C.; Wan, J.; Zhu, S.; Jacob, R. J.; Zhou, W.; Dai, J.; Wang, Y.; Danner, V. A.; Yao, Y.; Fu, K.; Wang, Y.; Bao, W.; Li, T.; Zachariah, M. R.; Hu, L. Ultra-Fast Self-Assembly and Stabilization of Reactive Nanoparticles in Reduced Graphene Oxide Films. *Nat. Commun.* **2016**, *7* (1), 12332.
(38) Jacob, R. J.; Kline, D. J.; Zachariah, M. R. Speed 2-Dimensional Temperature Measurements of Nanothermite Composites: Probing Thermal vs. Gas Generation Effects. *J. Appl. Phys.* **2018**, *123* (11), 115902.
(39) Song, J.; Chen, C.; Zhu, S.; Zhu, M.; Dai, J.; Ray, U.; Li, Y.; Kuang, Y.; Li, Y.; Quispe, N.; Yao, Y.; Gong, A.; Leiste, U. H.; Bruck, H. A.; Zhu, J. Y.; Vellore, A.; Li, H.; Minus, M. L.; Jia, Z.; Martini, A.; Li, T.; Hu, L. Processing Bulk Natural Wood into a High-Performance Structural Material. *Nature* **2018**, *554*, 224.
(40) Ku, H.; Wang, H.; Pattarachaiyakoop, N.; Trada, M. A Review on the Tensile Properties of Natural Fiber Reinforced Polymer Composites. *Composites, Part B* **2011**, *42* (4), 856−873.

https://doi.org/10.1021/acs.nanolett.0c03620
Nano Lett. 2021, 21, 4517−4523